Regular Article

Check for updates

Exploriting of graphene oxide for improving physical properties of TiO$_2$(NPs): toward photovoltaic devices and wastewater remediation approaches

O. O. Alameer[1], **A. Timoumi**[2,a], **N. El Guesmi**[3,b], **S. N. Alamri**[4], **W. Belhadj**[2,c], **K. Althagafy**[2], **Saleh A. Ahmed**[3,5]

[1] 4616, king Fahd, Makkah, Saudi Arabia
[2] Department of Physics, Faculty of Applied Science, Umm Al-Qura University, Makkah 21955, Saudi Arabia
[3] Department of Chemistry, Faculty of Applied Science, Umm Al-Qura University, Makkah 21955, Saudi Arabia
[4] Department of Physics, Science Faculty, Taiba University, Madinah, Saudi Arabia
[5] Chemistry Departement, Faculty of Science, Assiut University, Assiut 71516, Egypt

Abstract This work reports the impact of graphene oxide (GO) on titanium dioxide (TiO$_2$)-based thin films. The obtained data represent a methodical investigation on the physical and dielectric characteristics of TiO$_2$ nanoparticles (NPs) in solution mixed with different volumes of graphene oxide (0, 2, 4, 6 ml) and deposited on a glass substrate by spin coating. Our obtained nanocomposites films were characterized by FTIR, SEM, EDX, XRD, UV–Vis, thermogravimetric analysis and impedance spectroscopy (IS) techniques. The presence and disappearance of functional groups were confirmed by FTIR spectroscopy. SEM images displayed agglomerative surface and a remarkable correspondence between added content, the surface roughness and porosity of the films. The band gap energy of our GO–TiO$_2$ nanocomposites decreased in the range of 3.2–2.2 eV. The impedance spectroscopy analysis revealed a semiconducting behavior of layers after annealing until 150 °C. The photocatalytic activities of GO–TiO$_2$ nanocomposite were esteemed by degradation of methyl orange (MO) under UV-irradiation. Our results open up the opportunity for using the GO–TiO$_2$ nanocomposite thin films as promising candidate in solar cells or photovoltaic applications.

1 Introduction

Many initiatives have recently been made to produce and investigate various semiconductor [1–4], composites [5–9] and nanocomposites materials [10–12]. Titanium dioxide (TiO$_2$) is a polymorphic and semiconductor material, which was used as a pigment in several industries. The advent of sophisticated instruments and nanotechnology has encouraged the expenditure of TiO$_2$ for several applications such as in photocatalytic materials [13], antimicrobial surfaces [14], photochromic [15], photovoltaic cells [16], and gas sensors [17] by reducing the size of its particles. When graphene oxide and titanium dioxide are combined together, nanocomposite thin films are formed [18, 19] and used as window layer for a perovskite solar cell [20]. This is principally shaped by synthesizing GO through an adapted Hummer's approach and TiO$_2$ using a hydrothermal solution method [21–25].

In addition, graphene oxide (GO) can be synthesized in the form of nano-sheets [26], which are anionic two-dimensional materials [27]. Because of the large surface area, it improves both optical and mechanical properties of the composite [28]. GO also is a good conductor of electrons [29] and possesses hydrophilic properties [30], resulting in excellent catalyst support [31]. It is worth mentioning that TiO$_2$ thin films have good optical properties [32] and provide a high refractive index in both linear and nonlinear spectrum [33]. It can be used for wavelength corrections, optical switching, and other optics application [34–36]. Combination of TiO$_2$ with GO stipulates an opportunity to invent systems that can be useful in numerous features of energy [37] and ecological studies.

The synthetic mechanism of GO–TiO$_2$ nanocomposite thin films is complexed because of the nature of the reaction that happens throughout the process of application and deposition. The application of the composite on a glass substrate by means of spin coating technique found to be depending on the state of material whether it is applied as a polymer [38] or colloid [39], the rotation of the step process [40], the duration of deposition, the rate of solidification of the deposits [41], and the concentration to be applied [42].

The main objective of the current work is to analyze the physical and optical properties of GO–TiO$_2$ nanocomposite thin layers deposited on glass substrates. We will also, explore their photocatalytic performances in the photodegradation of MO indicator under continuous UV irradiation.

[a] e-mail: aoteoume@uqu.edu.sa (corresponding author)

[b] e-mail: naguesmi@uqu.edu.sa (corresponding author)

[c] e-mail: wbbelhadj@uqu.edu.sa (corresponding author)

Fig. 1 Schematic representation of the synthesis of GO–TiO$_2$ nanocomposites thin films
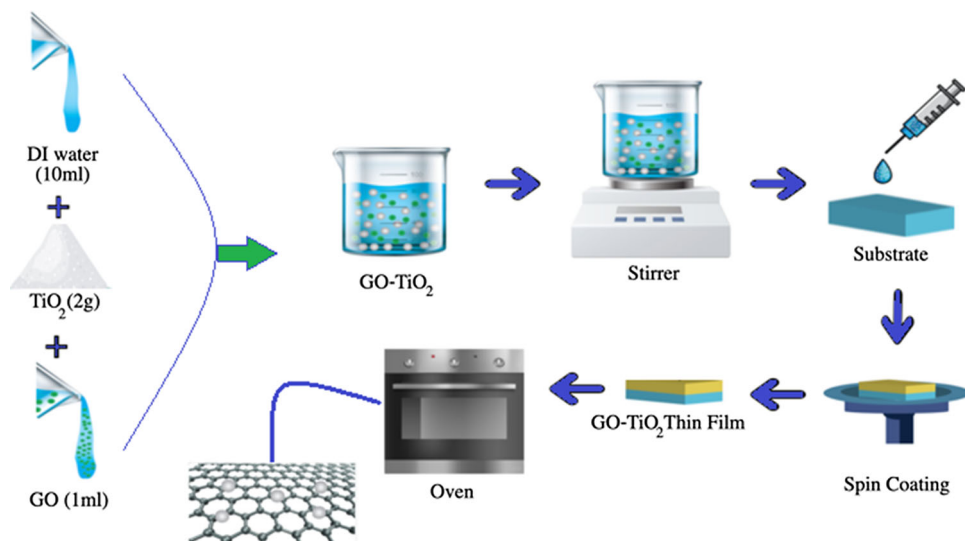
2 Synthesis and characterization methods

2.1 Materials synthesis

Firstly, we mixed 2.0 g of TiO$_2$ NPs in powder form (21 nm primary particle size (TEM)) ($\geq$ 99.5%) with 10 ml of deionized water and stirred at 27 °C for 30 min. Secondly, 2.0 ml of the obtained solution was dropped onto a cleaned glass substrate. Different amounts of graphene oxide (4, 8, 12 mg/ml) were added, and the resultant solution was mixed using a spin coating technique. The contemporary work predominantly intended to synthesize different percentages weight (wt) (0.2–0.6 wt.%) of graphene oxide (GO) and TiO$_2$ nanomaterial. Each different solution was fabricated in a distinct stage process alternated at 6000 RPM for 30 s. Then, each sample is heated a few minutes to dry as in Fig. 1. Finally, GO–TiO$_2$ nanocomposite thin films were obtained and analyzed as a function of content of GO.

2.2 Characterization methods

To analyze the structure of TiO$_2$ (NPs) and different concentration of GO–TiO$_2$ nanocomposite thin films, Fourier transform infrared spectroscopy (FTIR, Shimadzu IRSpirit) was successfully employed. The surface morphology was inspected by scanning electron microscopy (SEM, thermoscientific). The transmission and the absorption spectra were given by ultraviolet–visible spectropho-tometer (Thermo scientific, Evolution-201, UV–visible spectrophotometer). The impedance analyzer (Agilent 4294A) was used to determine the impedance parameters as a frequency function (10 Hz–13 MHz) at different temperatures (25–150 °C) of GO–TiO$_2$ nanocomposites samples. The (TGA) and (DTA) measurements were done using (DTG-60H, Shimadzu, Simultaneous DTA-TG Apparatus) in nitrogen atmosphere with heating rate 25–900 °C of 10/1 min.

2.3 Photocatalytic performances

The photocatalytic efficacy of our prepared samples was explored by measurement of the degradation rate of MO indicator as a typical contaminant under UV irradiation provided by a 125 W UV lamp placed vertically within 500 ml designed photochemical reactor. For all our assays, reaction suspensions have been produced by combining 30 mg of catalysts into a photoreactor comprising 370 mL with the concentration of 2×10^{-5} mol/L of the dye in aqueous solution and under continuous magnetically stirring (Fig. 2). The progress of the photocatalytic degradation of MO indicator has been recorded from its reduction in absorption intensity at the characteristic wavelength $\lambda_{max} = 464$ nm and at given time intervals of 5 min. Here we employed a computer aided double-beam Shimadzu 1800 using UV-VIS-NIR spectrophotometer having a resolution of 0.1 nm.

3 Results and discussion

3.1 FTIR analysis

The FTIR spectroscopy provides the functional groups of TiO$_2$ (NPs) and GO–TiO$_2$ nanocomposite thin layers in the wave-number range of (400–4000 cm^{-1}). Figure 3 displays the absorption peak at 434 and 742 cm^{-1} related to the Ti–O–Ti dilation at 890 cm^{-1}

Fig. 2 Experimental setup of photocatalytic reactor for degradation of MO dye
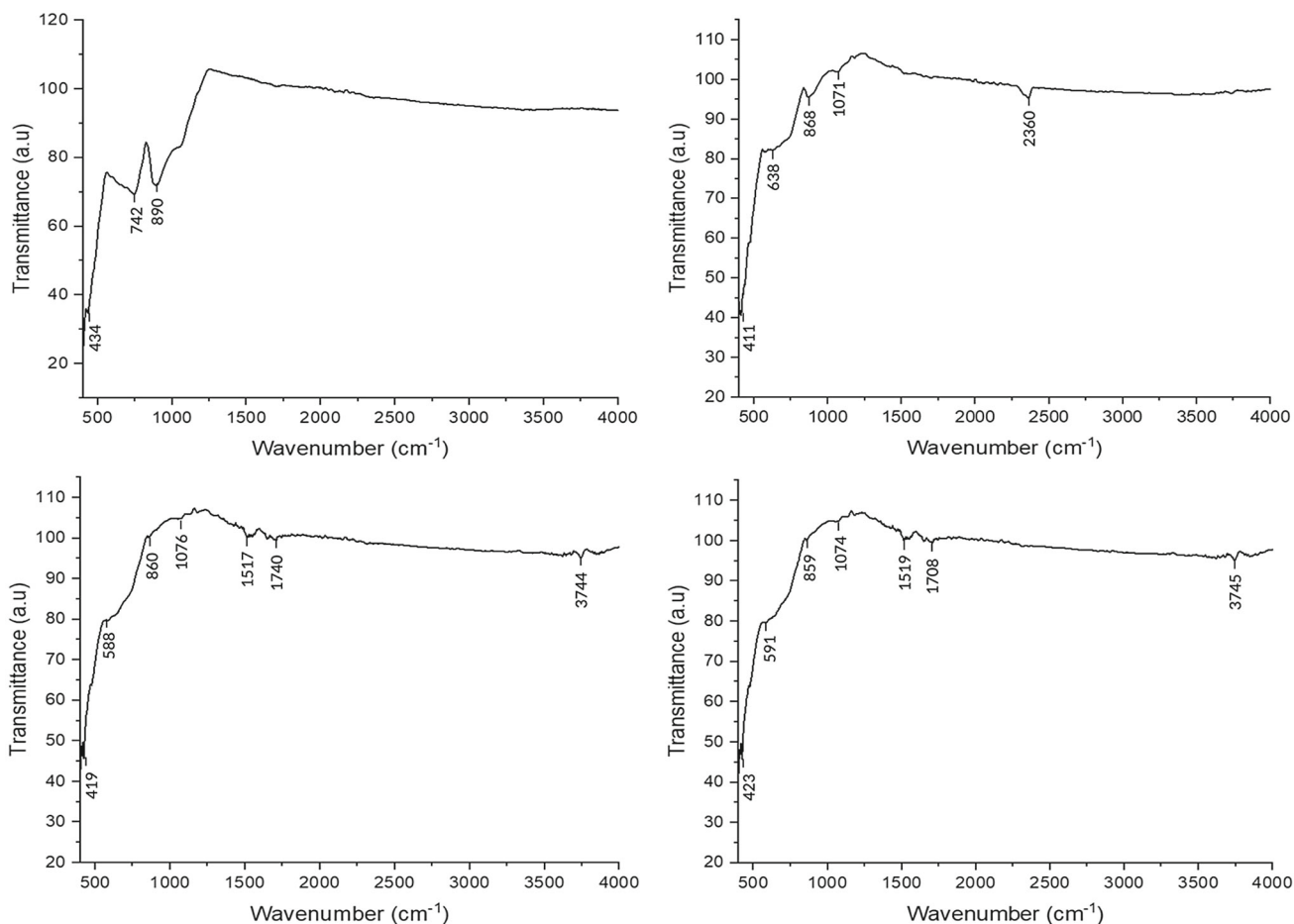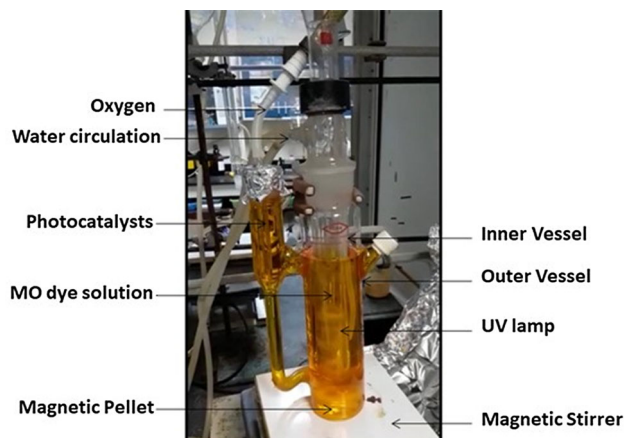
Fig. 3 FTIR spectra of **a** TiO$_2$ (NPs), **b** (0.2 wt.%) GO–TiO$_2$, **c** (0.4 wt.%) GO–TiO$_2$, **d** (0.6 wt.%) GO–TiO$_2$ nanocomposites thin films

associated to the Ti–O oscillation of TiO$_2$ (NPs) thin films. The attendance of the absorption bands at 411, 419, 423, 638, 588, 591, 868, 860 and 859 cm^{-1} is mainly ascribed to the stretching of Ti–O–Ti and Ti–O vibration of the different samples of GO–TiO$_2$ nanocomposites thin films [43–45]. In addition, the peaks in the interval of 400–1000 cm^{-1} are assigned to the stretching of Ti–O–Ti and Ti–O bonds of TiO$_2$ (NPs) [46].

Furthermore, the bands at 1071, 1076 and 1074 cm^{-1} are due to the stretching of C–O–C vibration [47]. The appearance of the peak at 2360 cm^{-1} related to O=C=O of GO–TiO$_2$ nanocomposites (0.2 wt.%) thin film [48]. However, by increasing the concentration led to appear the peaks at 1517, 1740 and 3744 cm^{-1} which belongs to C=C, C=O and O–H of GO–TiO$_2$ nanocomposites (4 ml) thin film, respectively. The peaks at 1519, 1708 and 3745 cm^{-1} were assigned to C=C, C=O and O–H, respectively of GO–TiO$_2$ nanocomposites (0.6 wt.%) thin film [49]. It is worth mentioning that, by, adding more concentration of GO–TiO$_2$ nanocomposites appears the hydroxyl and carbonyl groups which validate the existence of GO [50–53].
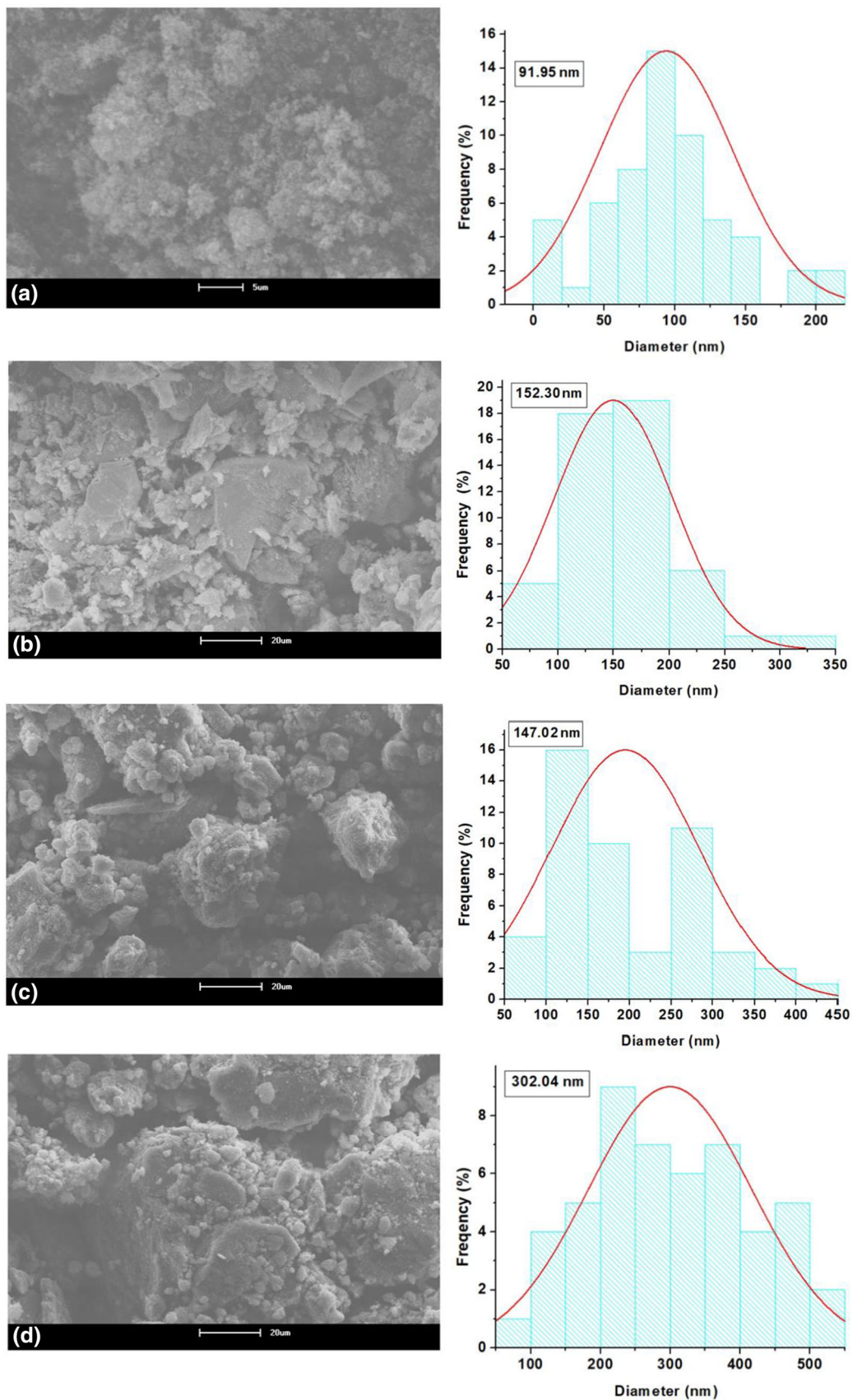
Fig. 4 SEM images and the grain size distribution of **a** TiO$_2$ (NPs), **b** 0.2 wt.%, **c** 0.4 wt.%, **d** 0.6 wt.% GO–TiO$_2$ nanocomposites thin films
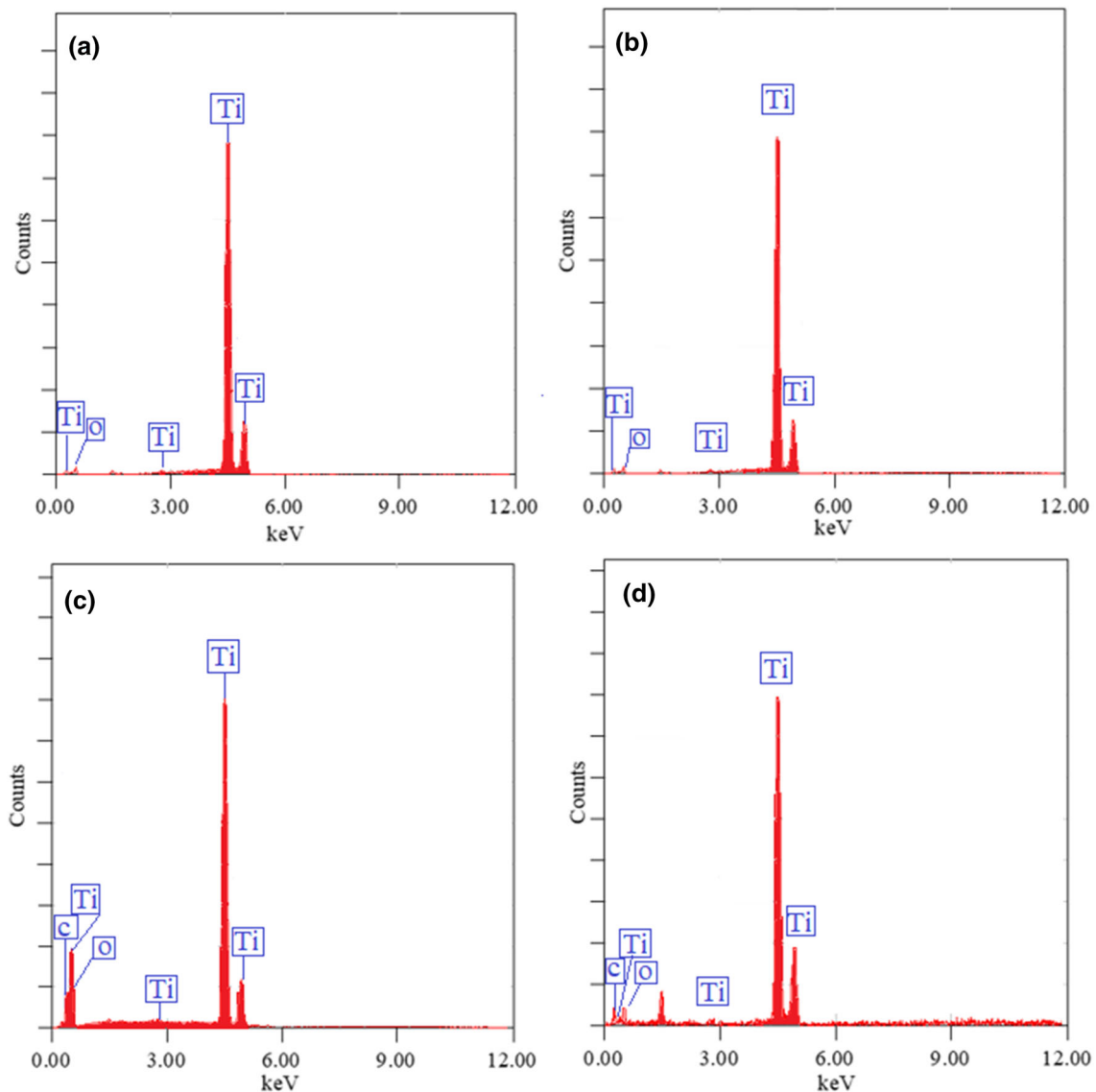
Fig. 5 EDX spectrum of **a** TiO$_2$ and of **b–d** GO–TiO$_2$ nanocomposite

3.2 Powder SEM, EDX and XRD characterizations

The morphology of TiO$_2$ and TiO$_2$ doped GO in the form of powder attained after the drying of the solutions was characterized by Scanning Electron Microscopy (SEM) and using Image J software to measure the nanoparticles size distribution. Figure 4a demonstrates a uniform surface of TiO$_2$ (NPs) thin film with average grain size 91.95 nm. Figure 4b–d represents a porous nature and by increasing the concentration of GO–TiO$_2$ thin films nanocomposites which led to increase the porous surface and the agglomeration. The other forms of agglomeration have been reported in the literature [15]. The average grain sizes of 0.2 wt.% GO–TiO$_2$ thin film nanocomposites are 152.30 nm and with 0.4 wt.% it reaches to 107.02 nm. By further increasing the concentration to 0.6 wt.%, the average grain size increases to 302.04 nm which is in agreement with [54]. The characterization of the chemical composition (Fig. 5) was carried out on the Powder sample by energy-dispersive X-ray (EDX) examination. The illustrative pattern (EDX) verifies the attendance of only Ti and O for the TiO$_2$ and only the existence of Ti, O and C for the GO-doped TiO$_2$ samples specifying the superiority and purity of our prepared samples. The X-ray diffraction (XRD) pattern indicates the crystalline nature of TiO$_2$ as well as GO–TiO$_2$ (Fig. 6) nanocomposite. A very intense characteristic peak (101) is obtained at 26° in the XRD diagram, this intensity decreases according to the addition of the GO probably serving for the appearance of the GO peaks for the GO–TiO$_2$ nanocomposite (Fig. 5b–d).
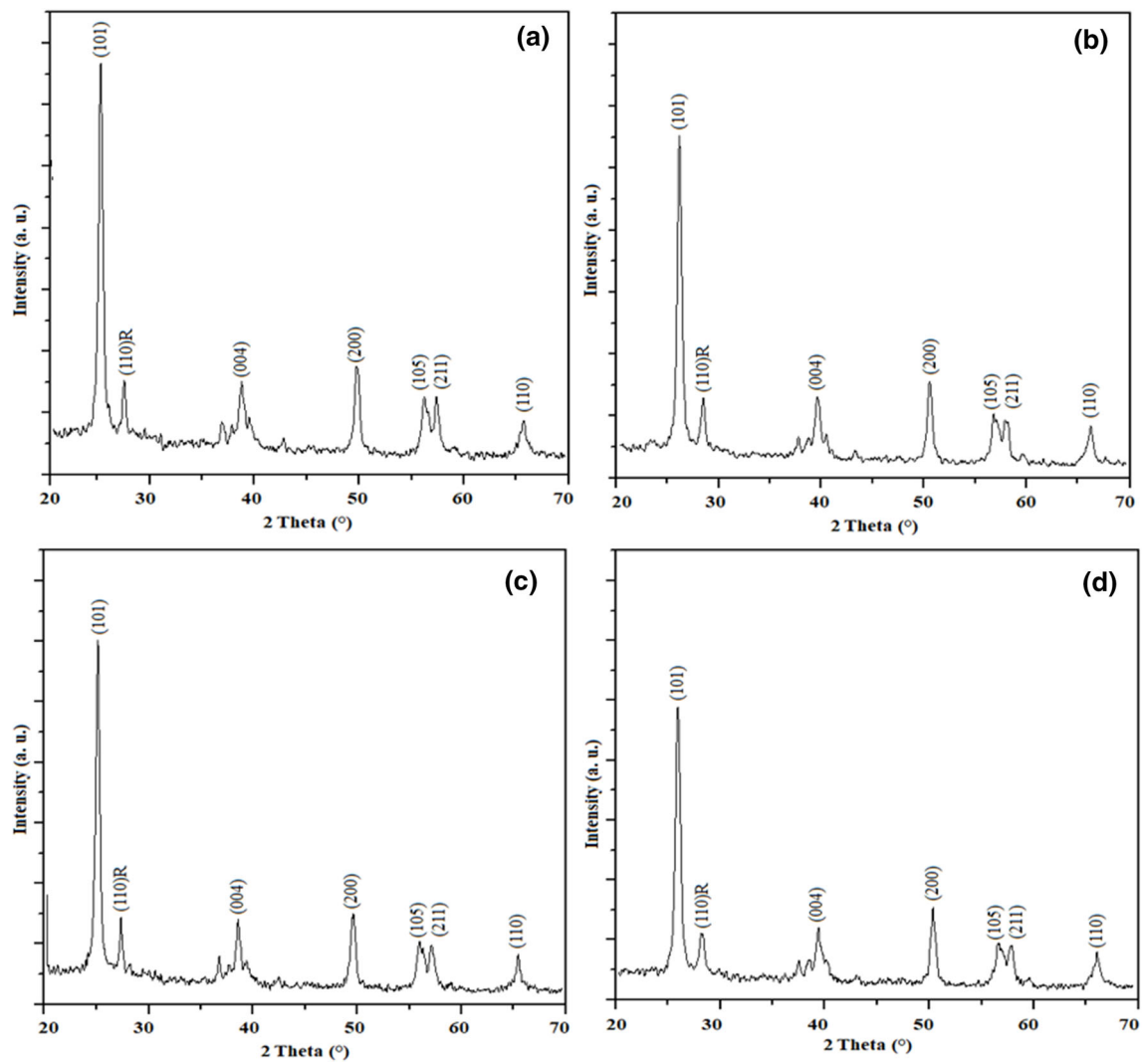
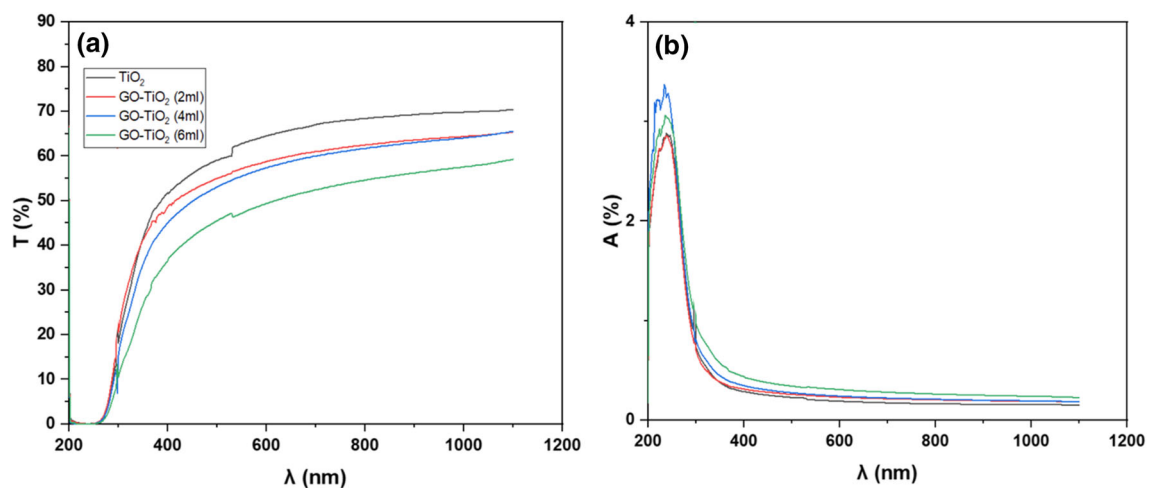**Fig. 6** XRD analysis of **a** TiO$_2$ and of **b–d** GO–TiO$_2$ nanocomposite

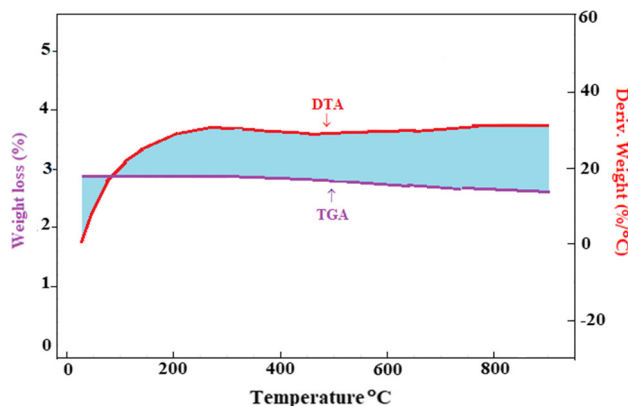**Fig. 7 a** UV–Visible Spectroscopy transmission and **b** absorption spectra

Table 1 The energy band gap of TiO_2 NPs and GO–TiO_2 nanocomposites thin films

Sample	TiO_2 NPs	(0.2 wt.%) GO–TiO_2	(0.4 wt.%) GO–TiO_2	(0.6 wt.%) GO–TiO_2
E_g (eV)	3.2	3.0	2.8	2.2

Fig. 8 Schematic representation of the charge transfer under UV–Vis irradiation and the variation of the optical band gap of **a** TiO_2 (NPs), **b** (0.2 wt.%), **c** (0.4 wt.%) and **d** (0.6 wt.%) GO–TiO_2 nanocomposites
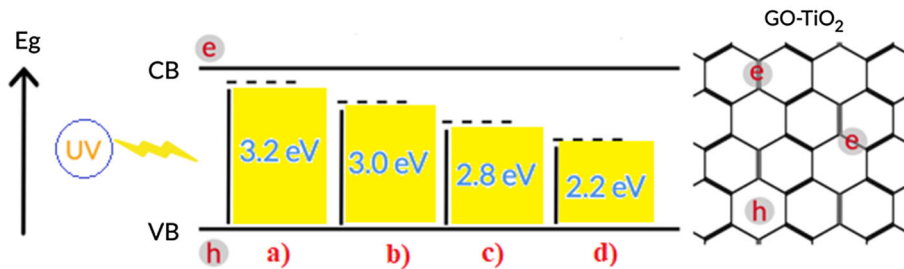
Fig. 9 Thermal analysis data (TGA) and (DTA)

3.3 Optical properties

Ultraviolet–visible (UV–VIS) spectroscopy was employed to study the Transmission (T) and Absorption (A) of TiO_2 (NPs) and GO–TiO_2 thin film samples shown in Fig. 7. The transparency result is about 70% of TiO_2 (NPs) thin films [55], and 62% of 0.2 wt.% and 0.4 wt.% GO–TiO_2 nanocomposites thin films. However, the transparency decreased to 56% of 0.4 wt.% GO–TiO_2 nanocomposite thin film.

To determine the energy band gap (E_g) of TiO_2 and GO–TiO_2 nanocomposites thin films we used the equation:

$$E_g = \frac{hc}{\lambda}$$
(1)

where h is the Planck constant, c is the speed of light and λ is the photon's wavelength. Table 1 summarizes the band gap energies of TiO_2 (NPs) and GO–TiO_2 nanocomposites. From this table it can be noted that the E_g-values are in the range of 3.0–2.2 eV for GO–TiO_2 nanocomposites samples which in good agreement with those reported in [56–58] (see Fig. 8). It is noticeable that, the increase in concentration of GO–TiO_2 nanocomposite led to a reduction in the energy band gap which is related to the change in the transparency and thickness.

3.4 Thermal analysis

Thermogravimetric analysis (TGA) and differential thermal analysis (DTA) measurements of the dielectric properties of TiO_2 (NPs) in a powder form, which measured in nitrogen atmosphere with heating range 25–900 °C, are shown in Fig. 9.

In DTA curve, the first loss below 150 °C is related to the water removal. Also, there is a low exothermic peak at 278 °C which is mainly attributed to oxidation decomposition. The exothermic peak at 567 °C is associated to the crystallization of TiO_2 anatase phase which in good conformity with the literature [59–61]. TGA curve stayed straight without weight loss till near 500 °C and then slight change without any weight loss.

3.5 Impedance spectroscopy analysis

Impedance Spectroscopy (IS) is successfully used to study the effects of the different temperature on the dielectric behavior of TiO_2 nanocomposites in pellet form. The Nyquist diagrams are analyzed as a frequency function (10 Hz–13 MHz) at different

Fig. 10 a The Nyquist plot of (Z' vs. $-Z''$) of TiO_2 nanocomposite in pellet form at different temperatures and **b** equivalent proposal circuit
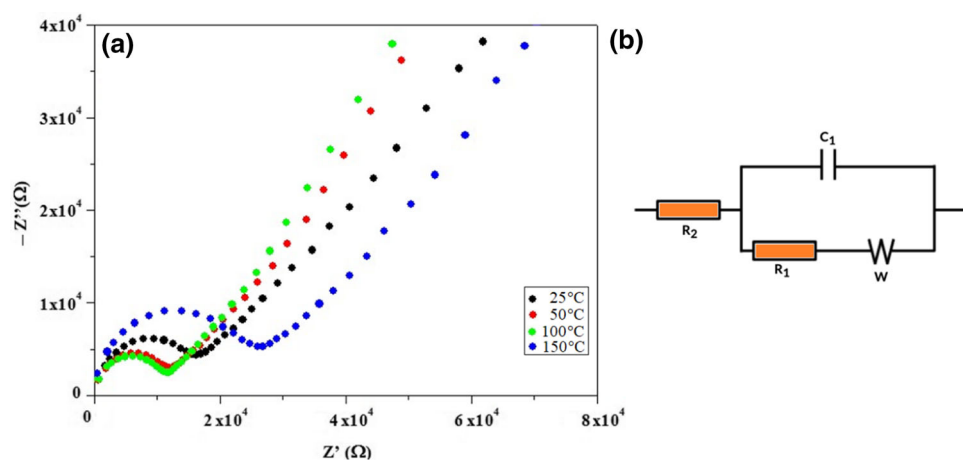
temperatures (25–150 °C). Figure 10a shows a semicircular shape at low-frequency component that ascribed to the recombination resistance (R_{ct}) and the values at high frequency component is associated to the charge transport resistance (R_{rec}) [62]. The different temperatures pretentious the semicircles' shape, which result a dependent on the temperature. The straight lines in the Nyquist plot are representing Warburg impedance correspond to the equivalent circuit model in Fig. 10b. Where the polarization is due to a combination of kinetic and diffusion processes.

3.6 Photocatalytic activity

The photocatalytic activities of GO–TiO_2 nanocomposite samples with (0.2 wt.%), (0.4 wt.%) and (0.6 wt.%) of GO were examined by the photodegradation MO indicator as a pollutant under UV illumination by 125 W UV-lamp. The photodegradation of the dye solution was kinetically followed by decreasing the absorbance and using UV–VIS spectrophotometer at definite time interval of 5 min with the whole period of photodegradation of from 0 to 80 min. Figure 11 reveals that the GO–TiO_2 thin films display high degradation which exceeds 60% for irradiation time of only 30 min. The percentage of degradation was computed using the formula:

$$\text{Deg.\%} = [(C_o - C_t)/C_o] \times 100 \qquad (2)$$

where C_o is the initial concentration of MO before irradiation and C_t is the concentration of the dye after irradiation time 't'. From Fig. 11 almost 60% of dyes have been degraded after 30 min of irradiation using pure TiO_2 (Deg.% = 61%), (0.2 wt.%) GO–TiO_2 (Deg.% = 60%), (0.4 wt.%) GO–TiO_2 (Deg.% = 59%), whereas it is only 50% for (0.6 wt.%) GO–TiO_2.

The Kinetics of photocatalytic degradation of MO was considered under UV irradiation at $C_o = 7$ mg/L $\sim 2 \times 10^{-5}$ mol/L, pH 7, and catalyst loading of 80 mg/L. The impact of dye concentration on the rate of degradation is summarized by the formula:

$$-\ln(C_t/C_o) = k.t \qquad (3)$$

where k is the rate parameter. To evaluate the rate parameter, the graphs of $-\ln(C_t/C_o)$ *vs.* time were plotted for the photodegradation of MO dyes with pristine TiO_2, (0.2 wt.%), (0.4 wt.%) and (0.6 wt.%) GO–TiO_2 nanoparticles as presented in Fig. 12. The calculated rate parameters are 0.0422, 0.0312, 0.0330 and 0.0248 min^{-1} for pristine TiO_2, (0.2 wt.%), (0.4 wt.%) and (0.6 wt.%) GO–TiO_2, respectively. This propensity was also recorded for Ag-doped TiO_2 NPs prepared by sol gel technique in which the rate parameters of pristine TiO_2, 5 mol % and 7 mol % Ag-TiO_2 catalysts were calculated to be 0.0403, 0.1595 and 0.0942 min^{-1}, respectively [63]. The obtained results remain interesting notably compared to other results cited in the literature, in which the photocatalytic degradation of MO, under UV irradiation using TiO_2 NPs synthesized by chemical vapor deposition method that displayed 69% of dye degradation in 6 h [64] and under sun light irradiation employing TiO_2 NPs synthesized by sol–gel technique in neutral medium followed by 87% of MO degradation after 3 h of irradiation [65]. But it remains less than the photocatalytic efficiency obtained for scoria-Ni/TiO_2 NPs that are about 96% and 94% for MO removal under both UV and sunlight irradiations, respectively, within only 45 min contact time [66]. Indeed, it was reported that the photocatalytic performance of TiO_2/GO composites was associated with that: (a) The GO is considered as an appropriated candidate to act as an electron acceptor owing to their distinguished mobility of charge carriers as well as charge trapping [67]. (b) When combination with GO, the charge recombination of TiO_2 can be remarkably inhibited by an electrons transfer toward GO, that produce more charge carriers, and thus forming species much reactive that favor the degradation of dyes [67]. Consequently, TiO_2/GO composites with a larger surface area can disperse uniformly in the solution, promoting the diffusion of molecules of dye (MO) to the surface of catalysts from solution, and thus enhance the performance photocatalytic [67].
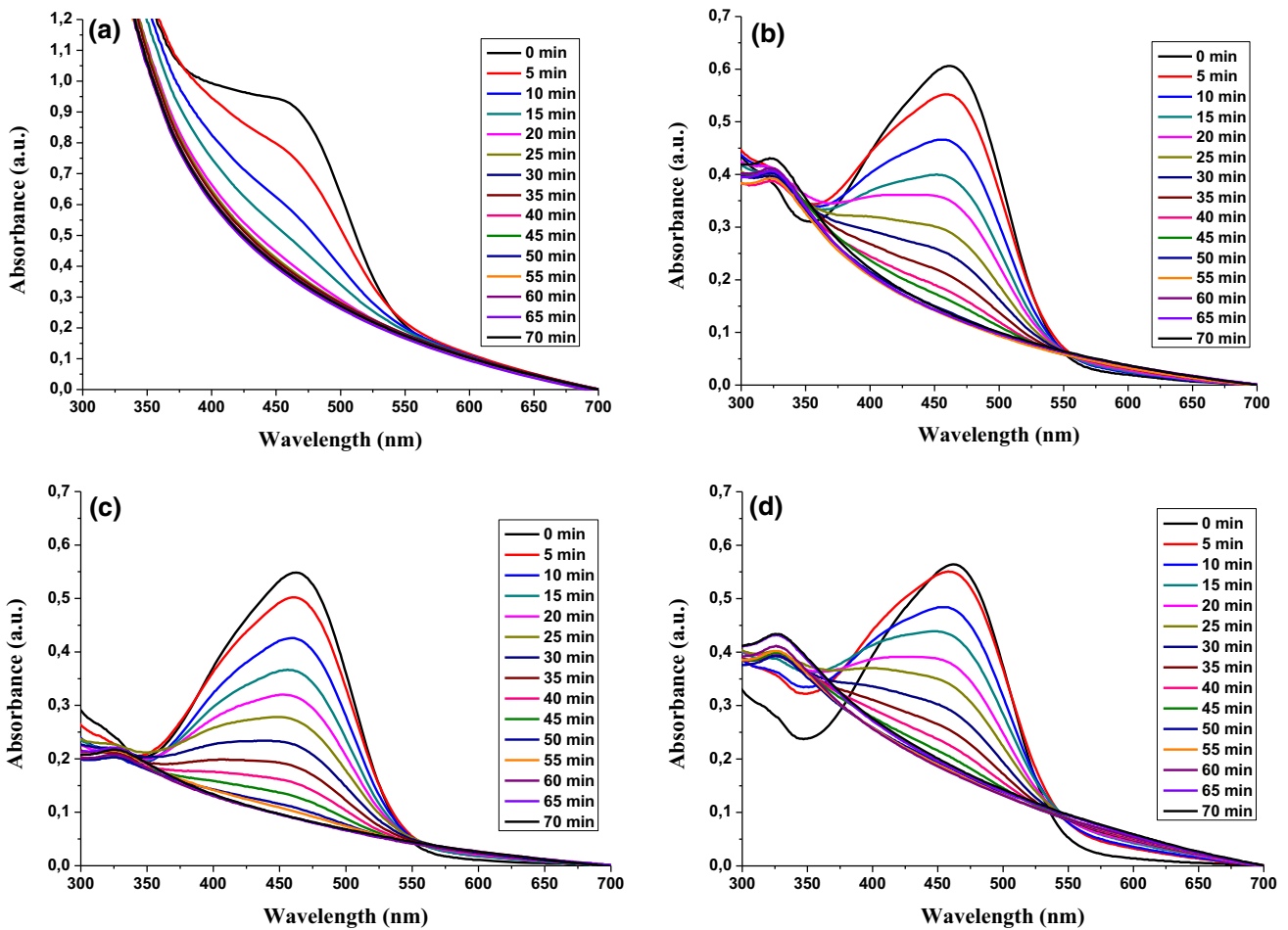
Fig. 11 The absorption spectra of the degradation of MO under UV light irradiation at different time intervals using **a** TiO$_2$ (NPs) **b** (0.2 wt.%), **c** (0.4 wt.%) and **d** (0.6 wt.%) GO–TiO$_2$ nanocomposites
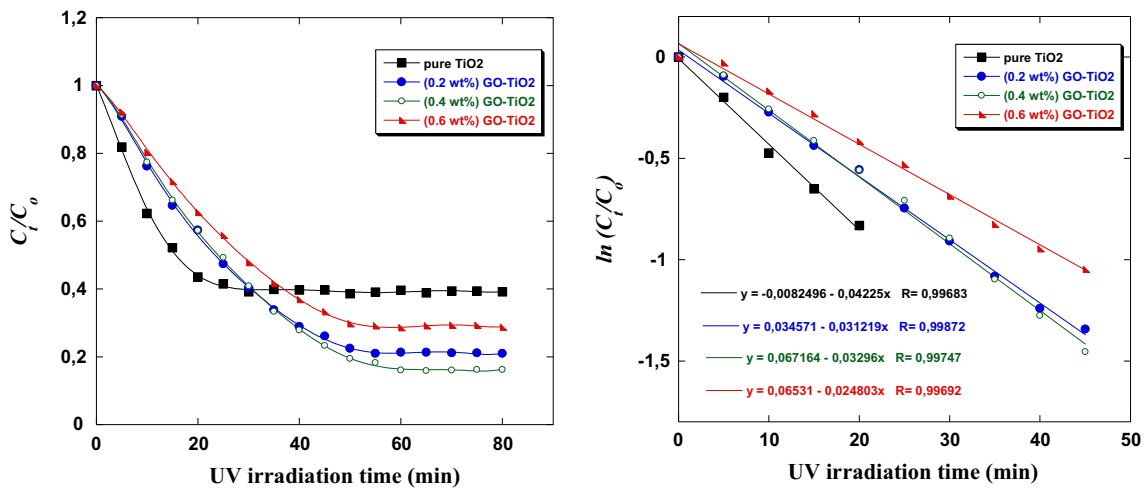

Fig. 12 The kinetic spectra of MO degradation using TiO$_2$ (NPs), (0.2 wt.%), (0.4 wt.%) and (0.6 wt.%) GO–TiO$_2$ nanocomposites

3.7 Photodegradation mechanism

The simplified proposed mechanism of MO catalyzed degradation [65, 68–73] demonstrates generation of electrons (e^-) and holes (h^+) in the conduction band (CB) and valence band (VB), respectively. Indeed, when TiO$_2$ NPs are irradiated with radiation energy greater than or equal to its band gap energy (3.2 eV) excitation in relation initiates to charge separation. When the GO–TiO$_2$ samples

Fig. 13 The mechanism of photocatalytic degradation of MO with GO–TiO$_2$ nanocomposites under UV-light irradiation
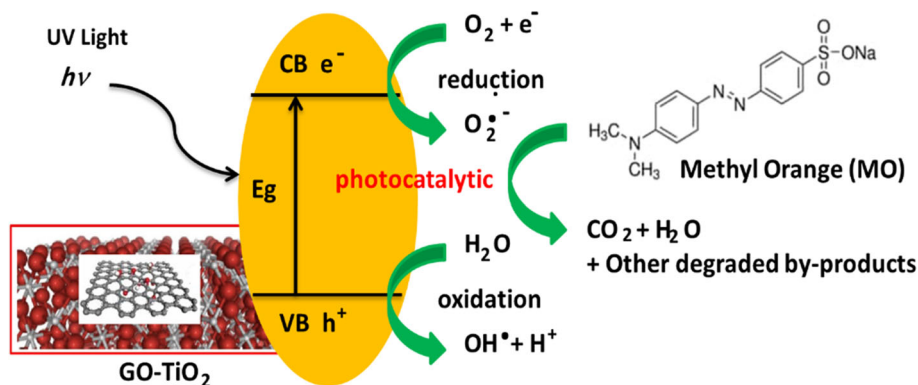
are irradiated by radiation energy greater than their band gap energies, this will lead to the production of excited e^-/h^+ pairs (CB electron e^-_{CB}, VB hole h^+_{VB}) manifesting with high-energy levels. Both h^+/e^- are looked as powerful oxidizing and reducing agents, respectively. The h^+_{VB} associated with the MO dye leads to its oxidation while awarding CO_2 and H_2O additional mineralization as end reducing it to superoxide radical anion $O_2^{\cdot-}$. Moreover, the generation of OH$^{\cdot}$ can be readily created by H_2O oxidation by interacting with h^+_{VB}. The generated OH$^{\cdot}$ exhibits large oxidation energy (2.80 eV), which is able to oxidize the majority of MO organic particles generous with e^- transforming them to non-toxic end products such as water and Carbone dioxide (Fig. 13).

4 Conclusions

In this work, a spin coating method was successfully applied to synthesize GO–TiO$_2$ nanocomposite thin films. The study was carried out using different concentration of GO in TiO$_2$ to obtain nanocomposite thin films on the optical and dielectric properties. The existence of oxygen functional groups with increasing of the concentration is detected. SEM photographs displayed a progressive genesis of dense thin films released of cracks with increasing the proportion of GO. Our computed gap energies are in the interval 3.20–2.2 eV for TiO$_2$ (NPs) and GO–TiO$_2$ nanocomposite thin films. The thermal result showed a dense and anatase phase around 567 °C. Our results reveal the significant impact of GO on the surface, optical and dielectric characteristics of TiO$_2$ nanocomposites. The pure TiO$_2$, (0.2 wt.%), (0.4 wt.%) and (0.6 wt.%) GO–TiO$_2$ nanocomposites have been employed as photocatalyst for the photocatalytic degradation of MO dye under UV irradiation. Our samples showed attractive photocatalytic rate of about 60% of dye degradation in only 30 min. The results displayed here may expedite the use of GO–TiO$_2$ materials for photovoltaic devices, as well as in the field of environmental photocatalysis toward clean water.

Author contributions All authors contributed to manuscript preparation.

Data availability The authors declare that all datasets supporting the findings of this study are available within the article.

Declarations

Conflict of interest The authors have no conflict of interest.

References

1. X. Yin, H. Huang, J. Xie, D. Dastan, J. Li, Y. Liu, X. Tan, X. Gao, W. Shah, X. Ma, Green Chem. Lett. Rev. **15**(3), 546–556 (2022)
2. I. Ashraf, S. Ahmad et al., Electrochim. Acta **429**, 141036 (2022)
3. I. Ashraf, S. Ahmad, F. Nazir et al., Int. J. Hydrog. Energy. **47**, 27383–27396 (2022)
4. X. Yin, W. Zhou, D. Dastan, J. Li, X. Tan, Y. Liu, X. Gao, X. Ma, Mater. Sci. Semicond. Process. **149**, 106886 (2022)
5. A. Alsulamei, A. Timoumi, Opt. Mater. X **15**, 100176 (2022)
6. M. Han, Z. Shi, W. Zhang, K. Zhang, H. Wang et al., Compos. Part A **149**, 106559 (2021)
7. H. Wang, Z. Huang, X. Li, Y. Zhou, Q. Yu, W. Hu, Y. Wang, W. Zhuang, D. Dastan, J. Alloys Compd. **920**, 166011 (2022)
8. W. Zhang, X. Zhu, L. Liang, P. Yin, P. Xie, D. Dastan, K. Sun, R. Fan, Z. Shi, J. Mater. Sci. **56**, 4254–4265 (2021)
9. Y. Jiao, Z. Huang, W. Hu, X. Li, Q. Yu, Y. Wang, Y. Zhou et al., Mater. Sci. Eng. A. **820**, 141 (2021)
10. X.-T. Yin, J. Li, Q. Wang et al., Langmuir **37**(46), 13548–13558 (2021)
11. N. Haghnegahdar, M. Abbasi Tarighat, D. Dastan, J. Mater. Sci. Mater. Electron. **32**, 5602–5613 (2021)
12. X. Yin, S. Wu, D. Dastan, S. Nie, Y. Liu, Z. Li, Y. Zhou, J. Li, A. Faik, K. Shan, Z. Shi, M. Abbasi Tarighat, X. Ma, Surf. Interfaces **25**, 101190 (2021)

13. A. Saleem, N. Ullah, K. Khursheed, T. Iqbal, S.A. Shah, M. Asjad, M. Arshad, J. Electron. Mater. **47**(7), 3749–3756 (2018)
14. X. Zhao, Z. Wang, Y. Xie, X. Haiyang, Z. Jiaxue, Z. Xintong, L. Weizhen, Y. Guochun, M. Jiangang, L. Yichun, J. Small. **14**(29), 1870136 (2018)
15. R. Eglitis, A. Zukuls, R. Viter, A. Šutka, J. Photochem. Photobiol. Sci. **19**(8), 1072–1077 (2020)
16. W. Vallejo, A. Rueda, C. Díaz-Uribe, C. Grande, P. Quintana, J. R. Soc. Open Sci. **6**(3), 181824 (2019)
17. H. Xu, M. Ding, S. Liu, Y. Li, Z. Shen, K. Wang, J. Polym. **117**, 198–207 (2017)
18. K. Biju, M. Jain, Meas. Sci. Technol. **18**(9), 2991–2996 (2007)
19. W. Belhadj, A. Timoumi, F.A. Alamer, O.H. Alsalmi, S.N. Alamri, Res. Phys **30**, 104867 (2021)
20. A. Ahmed, T. Ahamad, N. Ahmad, M. Khan, J. Mater. Chem. Phys. **238**, 121906 (2019)
21. N. Lv, Y. Li, Z. Huang, T. Li, S. Ye, D.D. Dionysiou, X. Song, J. Appl. Catal. B Environ. **246**, 303–311 (2019)
22. A. Azani, D.S. Che Halin, K.A. Razak, M.M.B. Abdullah, M.A.A.M. Salleh, N. Mahmed, V. Chobpattana, I.O.P. Conf, Ser. Mater. Sci. Eng. **572**, 012079 (2019)
23. A. Mohan Das Gandhi, K. Soorya Prakash, V. Kavimani, J. Anti Corros. Methods Mater. **65**(4), 375–382 (2018)
24. P. Rani, A. Ghorai, S. Roy, D. Goswami, A. Midya, S. Ray, J. Mater. Res. Express. **6**(12), 125546 (2020)
25. B. Satheesan, A. Mohammed, J. Wear. **466–467**, 203560 (2021)
26. S. Saadi, B. Nazari, J. Compos. Compd. **1**(1), 34–38 (2019)
27. G.H. Jetani, M. Rahmani, EPJ Plus **135**(9), 1–21 (2020)
28. O. Akhavan, E. Ghaderi, J. Nanoscale. **5**(21), 10316 (2013)
29. P. Conti, E. Scopel, E. Leite, C. Dalmaschio, J. Mater. Res. **35**(21), 3012–3020 (2020)
30. P. Deb, J. Dhar, J. IEEE Photonics Technol. Lett. **31**(8), 571–574 (2019)
31. X. Dong, X. Liang, Y. Zhou, K. Bao, D.E. Sameen, S. Ahmed, Y. Liu, J. Biol. Macromol. **177**, 135–148 (2021)
32. D. Elahe, H. Alireza, J. Clin. Med. Rev. Case Rep. **5**(8), 228 (2018)
33. Z. Jie, X. Xiao, Y. Huan, H. Youkang, Z. Zhiyao, J. Environ. Technol. **42**(2), 193–205 (2019)
34. A. Kumar, L. Rout, L. Achary, A. Mohanty, R. Dhaka, P. Dash, RSC Adv. **6**(38), 32074–32088 (2016)
35. W. Liu, X. Yan, Q. Xue, J. Mater. Chem. C **1**(7), 1413 (2013)
36. R. Mathew, S. Kanmani, J. Water Pract. Technol. **15**(3), 645–651 (2020)
37. A. Timoumi, S.N. Alamri, H. Alamri, Res. Phys. **11**, 46–51 (2018)
38. M. Aziz, N.F.T. Arifin, W.J. Lau, Malays. J. Anal. Sci. **23**(3), 479–487 (2019)
39. M. Rezaei, S. Salem, Int. J. Chem. Kinet. **48**(10), 573–583 (2016)
40. R. Singh, R. Kumar, A. Kumar, D. Kumar, M. Kumar, J. Mater. Res. Express. **6**(10), 105621 (2019)
41. R. Singh, R. Kumar, A. Kumar, D. Kumar, M. Kumar, J. Elect. Mater. **49**(8), 4872–4881 (2020)
42. J. Vidya, P. Balamurugan, J. Desalin. Water Treat. **156**, 349–356 (2019)
43. S.A. Kazmi, S. Hameed, A.S. Ahmed, M. Arshad, A. Azam, J. Alloys Compd. **691**, 659–665 (2017)
44. W. Low, V. Boonamnuayvitaya, J. Environ. Manag. **127**, 142–149 (2013)
45. C.G. Silva, J.L. Faria, J. Photochem. Photobiol. Sci. **8**(5), 705 (2009)
46. L. Hongbin, Z. Youzhen, V. Sascha, T. Shaochun, M. Xiangkang, J. Sci. China Technol. Sci. **55**(4), 894–902 (2012)
47. M.H.H. Ali, A.D. Al-Afify, M.E. Goher, Egypt. J. Aquat. Res. **44**, 263–270 (2018)
48. M. Sharma, Nihal. J. Mater. Today Proc. **26**, 3390–3396 (2020)
49. X. Qiu, Z. Hong, J. Hu, L. Chen, X. Chen, X. Jing, J. Biomacromol. **6**, 1193–1199 (2005)
50. S.J. Bu, Z.G. Jin, X.X. Liu, L.R. Yang, Z.J. Cheng, J. Eur. Ceram. Soc. **25**(5), 673–679 (2005)
51. R. Rahimi, S. Zargari, Z. S. Shojaei, MDPI Conference Paper. (2014).
52. A. Wiatrowski, M. Mazur, A. Obstarczyk, J. Coat. **8**(11), 412 (2018)
53. S.H. Nam, S.J. Cho, J.H. Boo, J. Nanoscale Res. Lett. **7**(1), 1–6 (2012)
54. D. Susanti, M. Nafi, H. Purwaningsih, R. Fajarin, G.E. Kusuma, Proc. Chem. **9**, 3–10 (2013)
55. A. Timoumi, H. Albetran, H. Alamri, S. Alamri, I. Low, J. Superlattices Microstruct. **139**, 106423 (2020)
56. C. Dette, M.A. Pérez-Osorio, C.S. Kley, P. Punke, C.E. Patrick, P. Jacobson, K. Kern, J. ACS Nano Lett. **14**, 6533–6538 (2014)
57. H. Saleem, A. Habib, J. Alloys Compd. **679**, 177–183 (2016)
58. J. Aljuaid, A. Timoumi, S.N. Alamri, Opt. Mater. X, 100178 (2022).
59. E.T. Bekele, B.A. Gonfa, O.A. Zelekew, H.H. Belay, F.K. Sabir, J. Nanomater. **2020**, 1–10 (2020)
60. M. Lal, V. Chhabra, P. Ayyub, A. Maitra, J. Mater. Res. **13**(5), 1249–1254 (1998)
61. D. Tejero-Martin, Z. Pala, S. Rushworth, T. Hussain, J. Ceram. Int. **46**(4), 5098–5108 (2020)
62. D. Liu, J. Yang, T. Kelly, J. Am. Chem. Soc. **136**(49), 17116–17122 (2014)
63. M.R. Meghana, A.H. Deepa, R. Ravishankar, Int. J. Eng. Res. Technol. **8**, 675–680 (2019)
64. R. T. Bento, M. F. Pillis, (Chapter 11) 211–225 (2018).
65. P.P. Subha, M.K. Jayaraj, J. Exp. Nanosci. **10**, 1106–1115 (2015)
66. M. Pirsaheb, H. Hossaini, S. Nasseri, N. Azizi, B. Shahmoradi, T. Khosravi, J. Nanostruct. Chem. **10**, 143–159 (2020)
67. C.-J. Cai, M.-W. Xu, S.-J. Bao, C.-C. Ji, Z.-J. Lu, D.-Z. Jia, Nanotechnology **24**, 275602 (2013)
68. M.H.H. Ali, A.D. Al-Afify, M.E. Goher, Egypt. J. Aquat. Res. **44**, 263–270 (2018)
69. M.N. Rashed, A.A. El-Amin, Int. J. Phys. Sci. **2**, 73–81 (2007)
70. A. Fujishima, X. Zhangb, D.A. Tryk, Surf. Sci. Rep. **63**, 515–582 (2008)
71. M. Masahiko, W. Teruyoshi, Surf. Coat. Tech. **201**, 9309–9312 (2007)
72. C.G. Silva, J.L. Faria, J. Mol. Catal. A Chem. **305**, 147154 (2009)
73. S. Chin, E. Park, M. Kim, J. Jurng, Powder Technol. **201**, 171–176 (2010)